Evaporation decay and associated gamma multiplicity for ^{204}Rn via three fusion channels

R. Rohe, A. DiRienzo,* H. Enge, M. K. Salomaa, and A. Smith

Massachusetts Institute of Technology, Laboratory for Nuclear Science, Cambridge, Massachusetts 02139

W. Schier

University of Lowell, Lowell, Massachusetts 01854

N. Tsoupas

Yale University, A. W. Wright Nuclear Structure Laboratory, New Haven, Connecticut 06511

H. E. Wegner

Tandem Van de Graaff, Brookhaven National Laboratory, Upton, New York 11973

Near-barrier excitation functions for 2n, 3n, 4n, 5n, 2n1p, 3n1p, and 4n1p evaporation from ^{204}Rn following the fusion of ^{35}Cl+^{169}Tm, ^{48}Ti+^{156}Gd, and ^{65}Cu+^{139}La are compared between reactions and with statistical decay codes. First and second gamma multiplicity moments were obtained for all three systems at 50 MeV excitation energy. General agreement with statistical decay code predictions is found in all cases.

I. INTRODUCTION

This work is a study of evaporation residue cross sections associated with 2n, 3n, 4n, 5n, 2n1p, 3n1p, and 4n1p emission from the ^{240}Rn* compound nucleus following the fusion of ^{35}Cl+^{169}Tm, ^{48}Ti+^{156}Gd, and ^{65}Cu+^{139}La. Excitation functions for these processes were measured and compared in the excitation range of 30–70 MeV. Gamma multiplicity measurements were taken at 50 MeV excitation energy for each of the three systems.

The purpose of these studies was fourfold: (1) to look for entrance channel effects in the decay, equilibrium or otherwise, from the compound system;[1] (2) to test the cold nucleus[2] idea, which says that, in cases of strong fission competition (applicable for superheavy systems), the entrance channel which produces the least excitation energy in the compound nucleus at the Coulomb barrier would have the greatest chance of surviving against fission; (3) to check the reliability of statistical evaporation codes, specifically ALICE (Ref. 3) and MBII (Ref. 4), in this region; and (4) to examine the feasibility of obtaining evaporation residue spin distributions, through multiplicity measurements, for these low cross-section and low spin reactions. A relative comparison of these gamma multiplicity moments, between the three reactions, will be presented.

II. EXPERIMENTAL METHOD

The ^{35}Cl, ^{48}Ti, and ^{65}Cu ion beams were provided by the Brookhaven National Laboratory (BNL) Tandem Van de Graaff facility. The beam energies ranged from 145 to 185 MeV for ^{35}Cl, 210 to 235 MeV for ^{48}Ti, and 267 to 313 MeV for ^{65}Cu. Currents ranged from 0.5 particle nanoamperes (particle nA) for ^{48}Ti to 7 particle nA for

^{35}Cl. The targets were 270 to 800 μg/cm^2, having variance within a given system for different runs. Relevant target data are given in Table I. The data acquisition[5] and Sigma 7 computer at the facility were used for signal handling. Event mode recording and on-line single-spectrum displays were used for real time monitoring of events.

A. Excitation functions

The basic method for obtaining excitation functions is described by Schier et al.,[6] where the ^{37}Cl+^{169}Tm excitation functions were measured with the same instrument and procedure used in these measurements. Briefly, the evaporation residues are separated from the primary beam by an offset velocity selector.[6,8] They are then stopped by a silicon surface-barrier detector and, subsequently, alpha decay, leaving an energy signal which identifies the iso-

TABLE I. Target thickness and composition data for multiplicity and excitation function experimental runs.

	Run	τ (μg/cm^2)	Composition
^{169}Tm			
Evaporated on 5 μg/cm^2 formvar	Multiplicity Excitation	500 270	Natural abundance (100%)
^{156}Gd			
Rolled and self-supporting	Multiplicity Excitation	800 520,355	Enriched to 94%
^{139}La			
Rolled and self-supporting	Multiplicity Excitation	550 550,500	Natural abundance (99.9%)

tope and consequently the evaporation mode. In front of the solid state detector is a gas (isobutane) proportional counter which serves as an anticoincidence signal against multiple scattered beam and other background ions with energies similar to the decay alpha particles. The alphas did not trigger this device and so could be easily differentiated from the background.

In addition, the evaporation residues left a signal in the ΔE-E ion telescope which could easily be distinguished from those events already mentioned. This signal was used as a gate for the gamma multiplicity filter (Sec. II B), as well as a semi-independent means of obtaining the total evaporation residue cross section (Sec. III A). The total cross sections obtained by this method agreed well with the sum of the individual excitation functions found through the alpha decay analysis.

The velocity selector pivots about an axis through the target position so that angular distributions can be measured. Velocity distributions are obtained by properly adjusting the electric and magnetic fields of the velocity filter and quadrupole lenses. The beam intensity was monitored by two surface barrier detectors housed in the target chamber at 21.75 deg for Rutherford scattering normalization. The velocity filter is drawn schematically in Fig. 1. The absolute efficiency measured by Schier et al. for the velocity selector was used with these ^{35}Cl $+$ ^{169}Tm measurements because of the kinematic similarity with the ^{37}Cl $+$ ^{169}Tm reaction. The absolute efficiencies for the other two systems were obtained by an extrapolation procedure using the code RAYTRACE (Ref. 7) as well as empirical methods described previously.[8] Effective solid angles used were 0.52, 0.61, and 0.70 msr for Cl + Tm, Ti + Gd, and Cu + La, respectively.

B. Gamma multiplicities

The multiplicities were measured with an array of seven 7.6×7.6 cm NaI detectors surrounding the target chamber (Fig. 2). Each was housed in a lead shield to minimize Compton scattering cross-talk between detectors. The ar-
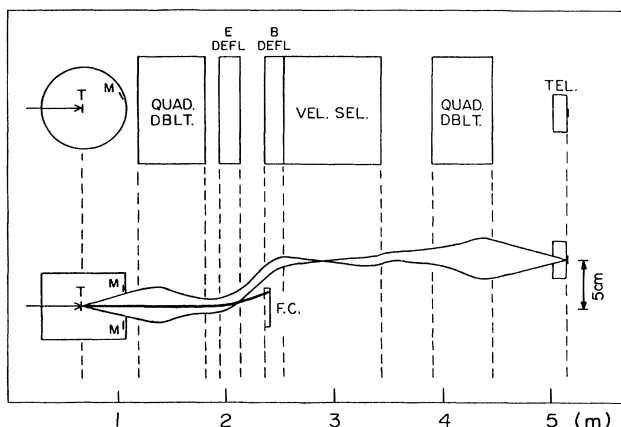

FIG. 1. A schematic view of the velocity-selector filter in the vertical plane. Shown are the target (T), monitors (M), Faraday cup (F.C.), quadrupole doublets, field deflection regions, and ΔE-E ion telescope (TEL).
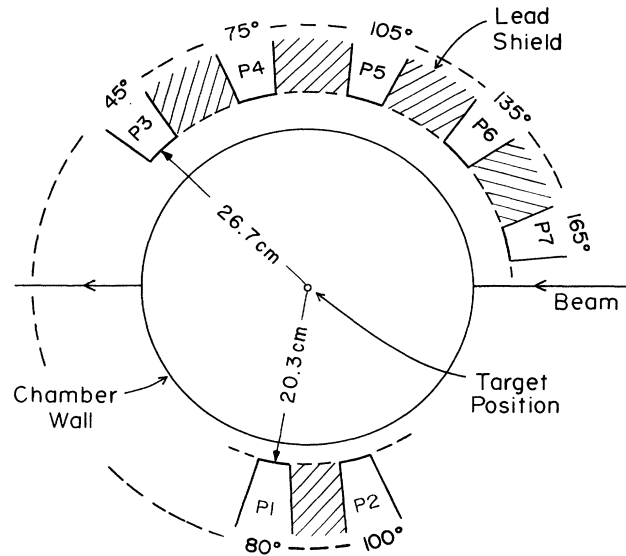

FIG. 2. NaI-photomultiplier detector arrangement. All detectors were in the horizontal plane of the beam line. Most of the detector faces looked through a thin slide strip in the chamber wall.

ray was read in delayed coincidence with the arrival of an evaporation residue at the rear of the velocity selector. The multiplicities were taken only at 50 MeV excitation and zero degree, zero percent $\Delta v/v$ [$0°,0\%(\Delta v/v)$] for all three systems ($\Delta v/v$ is the fractional difference between the center-of-mass velocity and that for which the velocity selector has been tuned). As a consequence of these two facts, only 3n, 4n, 2n1p, and 3n1p evaporation modes feed the spin distribution whose multiplicity moments were recorded. The $xn1\alpha$ distributions have a minimum at these "coordinates" [$0°,0\%(\Delta v/v)$] since the residues receive a recoil "kick" from the evaporated alpha particle which removes them from the acceptance window of the apparatus at these coordinate settings.

The "pattern" spectrum [which detector(s) fired] was recorded as a seven bit binary number, one bit per detector, for each event. Also, a time of flight spectrum was taken as further verification that the γ's came from the evaporation residues. The stop and start signals came from a common, delayed "OR" gate of the NaI detectors and the evaporation residue signal, respectively. The time order of the two signals was reversed so that the time analyzer would not be excessively triggered by the strong gamma background (Coulomb excitation, fission fragment decay, etc.) firing the NaI array. The time of flight spectra had 50–100 nsec FWHM, which further limited the background contribution in the multiplicity to less than two percent. Each NaI detector had a graded absorber of Pb, Cd, and Cu in order to minimize the energy variation in the gamma detection efficiency.

The absolute efficiencies for each detector were measured with ^{133}Ba and ^{60}Co calibrated sources at the beginning of the experiment. Each source was placed in the target position to take into account all chamber shielding effects. Background residual gamma measurements were taken as well. An attempt was also made to check these
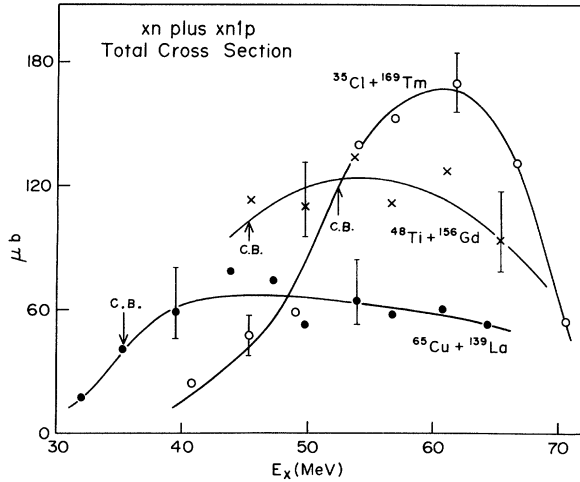
FIG. 3. Absolute cross sections for xn plus $xn1p$ evaporation modes. Near and below the barrier these are the only evaporation modes which contribute to the total residue cross section. See Sec. III D for error discussion. Curves in Figs. 3, 8—10 are drawn only to guide the eye, and their energy scales account for target losses.

efficiencies after the completion of the experiment, and an unreasonable discrepancy was found. Due to a lack of time, this discrepancy was not cleared up, so we have used the calibration data taken at the beginning of the run since these agree well with calculated efficiencies and there were no indications of major drifts during the run.

III. EXPERIMENTAL RESULTS AND ANALYSIS

A. Preliminary

The procedure in going from alpha decay spectra to absolute excitation functions is well described in the paper
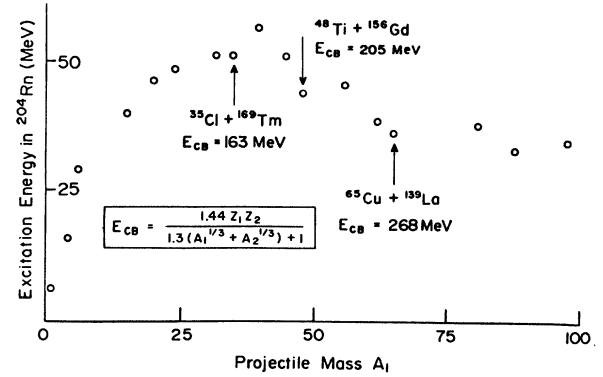

FIG. 4. Graph of the resulting ^{204}Rn excitation energy, formed at the "touching sphere" Coulomb barrier, for a variety of systems. Note the downward trend beyond $A=35$, particularly for the triad of reactions used in these measurements.

by Schier *et al.* The $xn1\alpha$ excitation functions are not included here because the error bars for those measurements are too large to extract any meaning from the data.

In Fig. 3 the $0°,0\%(\Delta v/v)$ residue data are summarized and fitted to a model recoil distribution resulting from xn and $xn1p$ evaporations in order to obtain the total absolute cross sections. These angular and velocity distributions were obtained from Monte Carlo simulations of the evaporation recoil profile[6] together with empirical verification at an intermediate energy for each system. The xn channels have a peak at $0°,0\%(\Delta v/v)$ and the $xn1p$'s have a slight minimum which is filled in by a convolution with the multiple scattering distributions. The xn angular distribution has a FWHM of about 4°, the $xn1p$ about 5°, and the $xn1\alpha$ about 12°, more or less as the center-of-mass

TABLE II. Spin moments extracted from ALICE and MBII statistical code calculations. Parameters used for both codes are as listed in Figs. 5 and 7 (both codes use these same parameter types).

Mode	Reaction	ALICE Mean ($\hbar$)	rms deviations	MBII Mean ($\hbar$)	rms deviations
3n	Cl + Tm	19.0	7.6	15.0	6.2
	Ti + Gd	19.5	7.8		
	Cu + La	17.6	8.4		
4n	Cl + Tm	15.1	6.5	11.2	5.2
	Ti + Gd	15.6	6.7	11.4	5.4
	Cu + La	15.2	6.9	11.4	5.4
2n1p	Cl + Tm	20.7	7.3	15.0	6.6
	Ti + Gd	21.7	7.5	15.6	6.7
	Cu + La	21.2	7.9	15.6	6.7
3n1p	Cl + Tm	15.1	6.5	10.7	5.1
	Ti + Gd	16.0	6.6	11.2	5.3
	Cu + La	15.8	6.7	11.3	5.4

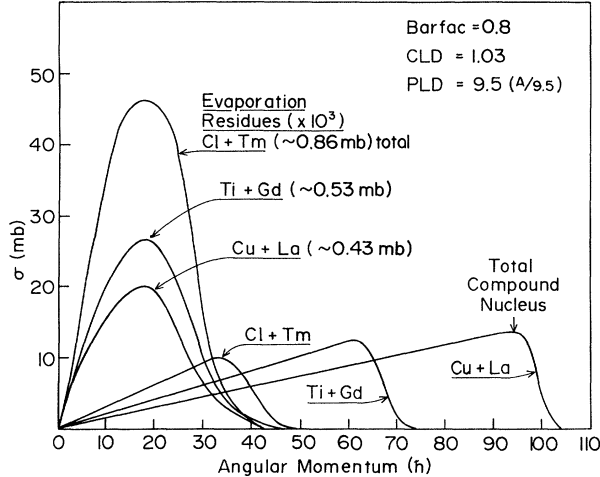|	MBII and ALICE Cl + Tm	Ti + Gd	Cu + La
E_x (MeV)	50.4	50.7	50.9
E_{lab} (MeV)	160.0	215.0	293.0

FIG. 5. ALICE (overlaid version) predictions for spin distributions of evaporation residues as well as total compound nucleus formation (residue and fission) at 50 MeV excitation energy. Overall absolute residue yield is very sensitive to CLD (fission to particle level density ratio) in regions of strong fission competition, and a small change of about 1% would bring the cross-section scale in line with our measurements. The relative yield for Cl + Tm has been overpredicted in this sensitive near-barrier energy regime for that system.

momentum is decreased or increased, respectively. At higher energies, the cross sections in Fig. 3 begin to turn downward. This dropoff is caused by the xn and $xn1p$ evaporation modes giving way to the $xn1\alpha$ modes and increased fission in this energy range.

In Fig. 4 the ^{204}Rn excitation energy is plotted as a function of different projectile masses (feasible systems chosen) for projectile-target center-of-mass energies corresponding to their classical Coulomb barrier. Except for extremely asymmetric systems, the cold nucleus idea would favor the symmetric systems for ^{204}Rn formation. This trend can be seen at higher projectile masses and specifically for the triad of reactions used in these measurements. The excitation energies corresponding to the Coulomb barrier are noted in Fig. 3 by the arrows labeled C.B. The results of these measurements show that the cross sections are just the opposite of what the "cold nucleus" idea predicts. The computer codes ALICE and MBII predict similar trends as the data.

B. Gamma multiplicities

ALICE-generated total spin distributions are shown in Fig. 5. First and second moments for individual evapora-

TABLE III. Measured gamma multiplicity moments at 50 MeV excitation and at 0° recoil direction. Only relative errors, arising from statistical uncertainty, are shown. Absolute errors are larger (see the text).

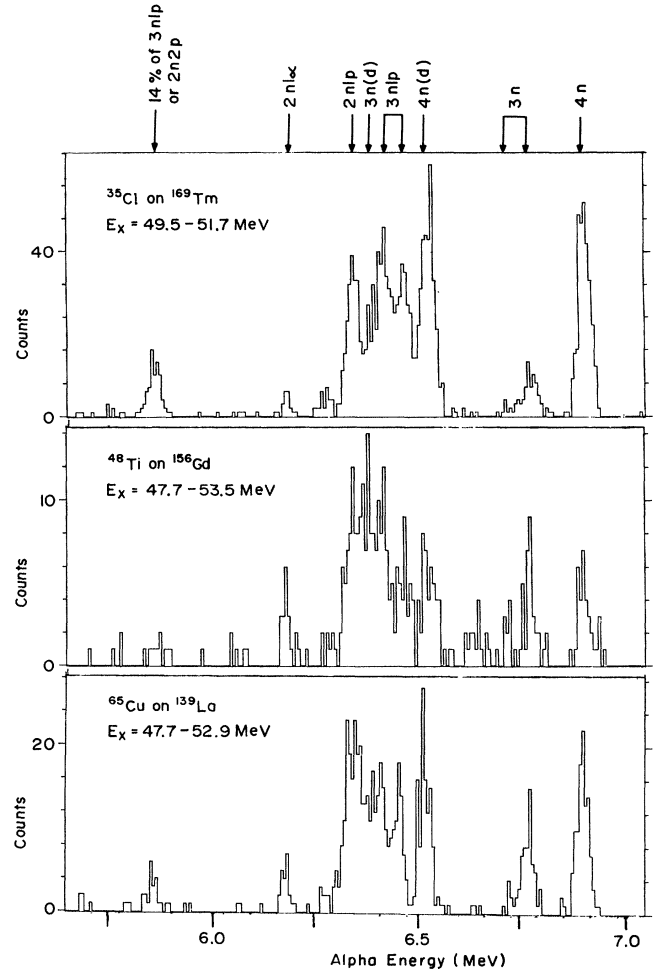| Reaction	Mean	rms deviations
Cl + Tm	8.69±0.31	4.94(+0.82−0.93)
Ti + Gd	9.31±0.74	2.7(+2.2−2.3)
Cu + La	8.66±0.19	3.33(+0.73−0.86)

FIG. 6. Alpha spectra from evaporation residue alpha decays within the 450 mm^2 silicon surface barrier detector. These spectra were collected at 0°,0%($\Delta v/v$) during the multiplicity runs (except Cu + La; see the text). (d) denotes α-daughter nucleus.

tion modes, as generated by ALICE and MBII, are listed in Table II. Since the code ALICE does not explicitly couple initial and final spins, the pre-evaporation and post-evaporation spin populations are identical for those nuclei which survive against fission. The MBII predicted spin moments are those corresponding to the distributions after the particle evaporation (and consequently the removal of some spin) has taken place. This results in lower spin means from MBII as compared with ALICE predictions (Table II). As can be seen, the means and root-mean square (rms) deviations are almost identical for all three systems. The small differences are partially due to the slightly different excitation energies used.

The three slopes of the partial cross sections $\sigma(L)$ to form the total compound nucleus (residue + fission) as generated by ALICE (Fig. 5), are proportional to the square of the reduced wavelength (λ^2) for the corresponding channels. This is the determining factor for the evaporation-residue cross-section ratios, producing the lowest value for Cu + La. The moments of the measured multiplicity distributions and their errors are listed in Table III. The moments were determined using the Van

TABLE IV. Alpha branching ratios used to obtain absolute cross sections.

Evaporation	Nucleus	E_α (MeV)	Ratio used	Source
2n	^{202}Rn	6.636	0.70	Ref. 11 (<0.70) Ref. 12 (0.85 ± 0.15)
3n	^{201}Rn	6.72	0.80	Ref. 11
	^{201}Rn^m	6.77	0.90	
4n	^{200}Rn	6.91	0.98	Ref. 11
5n	^{199}Rn	6.99	1.00	Estimate
	^{199}Rn^m	7.06	1.00	
2n1p	^{201}At	6.345	0.71	Ref. 13
3n1p	^{200}At	6.466 (60%) 6.415 (40%)	0.53	Ref. 13
4n1p	^{199}At	6.639	1.00	Estimate

der Werf formalism.[9] The errors given are relative errors, which here are only statistical in nature, assuming constant efficiencies for the NaI detectors throughout the run. If we assume negligible efficiency drift throughout the experiment, then the error of the absolute mean would be ±2.0 due to calibration uncertainty. This does not contribute to the error in a relative comparison between systems.

The similarity of the experimental multiplicity means supports the ALICE and MBII predictions if the average spin removed per gamma photon is assumed to be reaction independent. If the MBII predictions are correct, this average spin removal is about 1.4$\hbar$ per photon, which is a reasonable result in the low-spin regime. This result is readily obtained by taking a weighted average of the spin means in Table II and dividing by the multiplicities in Table III. The appropriate weighting of the means comes from Fig. 6 together with the branching ratios listed in Table IV. The errors on the second moments are much larger, but still lend support to the predicted widths. The distributions for the rest of the excitation range were predicted by ALICE to be similar as well. Since spin distributions are so similar, any major differences in evaporation cross-section ratios between the reactions would be attributed to pre-equilibrium or isomeric effects. (Major excitation function differences, due to spin distribution differences, were found by Gauvin *et al.*[10])

C. Excitation functions

Figure 6 is a direct comparison of the alpha spectra collected during the multiplicity runs. The decay data on the Cu + La multiplicity run was lost, but the spectrum shown here is from a shorter run taken immediately afterwards with identical apparatus settings. The energy ranges are due to variable beam energy loss within the target. For the most part, the overall trends are similar. The seemingly large differences in the 3n/4n counts ratio is due to the extreme sensitivity of these two excitation

peaks in this energy region. Such differences can arise within the beam loss and consequent excitation limits alone.

In Fig. 7 the excitation functions as predicted by ALICE are shown. A feature to notice is the similar evaporation cross-section ratios at a given energy, reflecting the simi-
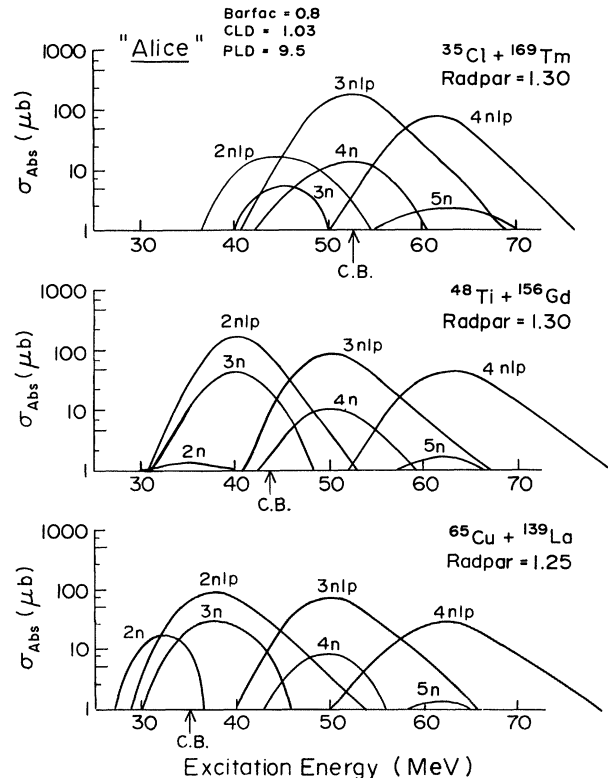

FIG. 7. Excitation functions generated by the statistical code ALICE (overlaid version). Note the branching ratio similarities for all three reactions. Except for "Radpar" we used the same parameter set for each system.
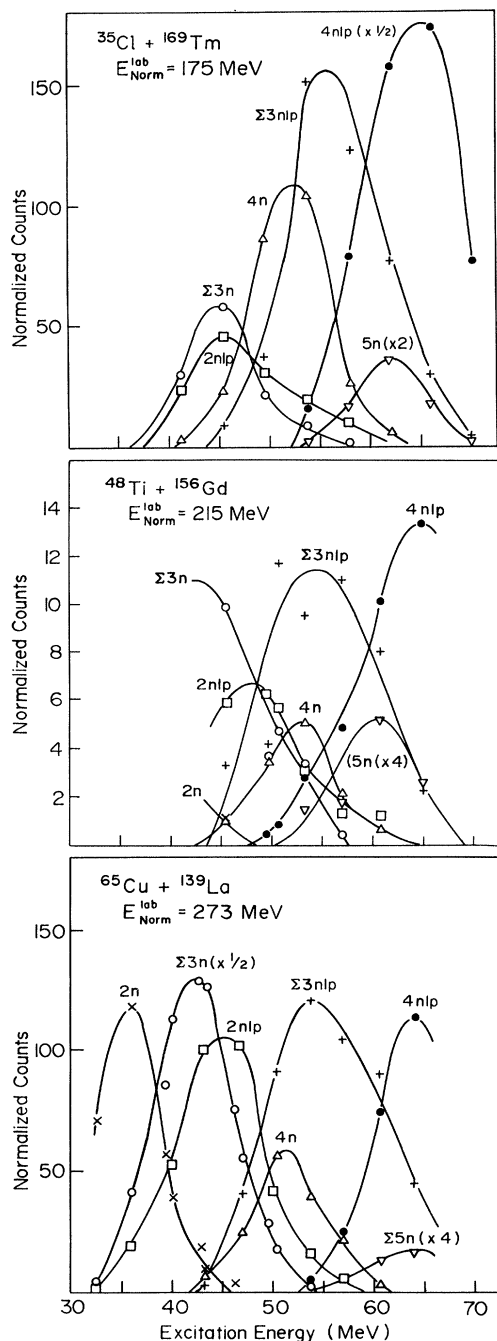
FIG. 8. Counts at $0°,0\%(\Delta v/v)$ normalized by the use of monitor counts and the Rutherford formula to represent relative cross sections, within each system, at $0°,0\%(\Delta v/v)$. Branching ratios have not been accounted for here. Angular and velocity distributions were taken at E_{NORM}^{lab} for all three reactions, and in addition, Cu + La had a second one taken at 293 MeV. Corresponding excitation energies are Cl + Tm 62, Ti + Gd 50, and Cu + La 37 and 50 MeV. Data counts obey Poisson statistics and their uncertainty can be found accordingly.

lar spin distributions. Also note the entrance channel (Coulomb barrier) effects which result in a large 2n cross section for Cu + La, but none for Cl + Tm. Another feature of interest is the long tail for $xn1p$ processes. This is due to the different order sequence for proton emission

holding up the cross section at higher energies.

The corresponding normalized data are presented in Fig. 8. All of these data were taken at $0°,0\%(\Delta v/v)$ and normalized by the monitor count of the Rutherford-scattered beam. These data are then normalized to absolute cross sections from velocity distributions measured at an intermediate energy in 1° or 2° steps around 0°. Integration of these angular distributions results in the cross sections for the corresponding energy. Appropriate scaling factors are then determined for each evaporation mode which in turn normalizes the data to absolute cross section for all energies. This procedure is described in detail in Ref. 6. The scaling ratio factors are found between the total counts after angle and velocity integrations and the normalized counts at $0°,0\%(\Delta v/v)$. This ratio will be largest for $xn1\alpha$ and smallest for xn. Since the $xn1\alpha$ minimum at $0°,0\%(\Delta v/v)$ is extremely sensitive to the setting of the electric and magnetic fields and varies greatly within our tuning error [due to the $xn1\alpha$ minimum at $0°,0\%(\Delta v/v)$ mentioned in Sec. II B], such a scaling is not very meaningful and the results are unreliable. Alpha energies and assumed branching ratios are listed in Table IV.

As an example of a velocity distribution, the velocity profiles for 3n, 4n, and $2n1\alpha$ emission from the Cu + La reaction are shown in Fig. 9. The 3n distribution is shifted slightly forward. This is an artificial effect caused by the fact that the 3n excitation function (Fig. 8) at $E_x = 50$ MeV has a strong downward slope. Combined with the large differences in stopping powers for the beam particle and the recoiling nucleus in the relatively thick target, this produces the observed shift.

Note also the asymmetry in the velocity profile for the $2n1\alpha$ evaporation. This asymmetry is proportional to $[1+(\Delta v/v)]^3$. One factor of $[1+(\Delta v/v)]$ arises from the fact that the absolute "bite" Δv of the velocity selector is proportional to v (about 6%).[6] By dividing out this factor and converting to center of mass, a symmetric distribution
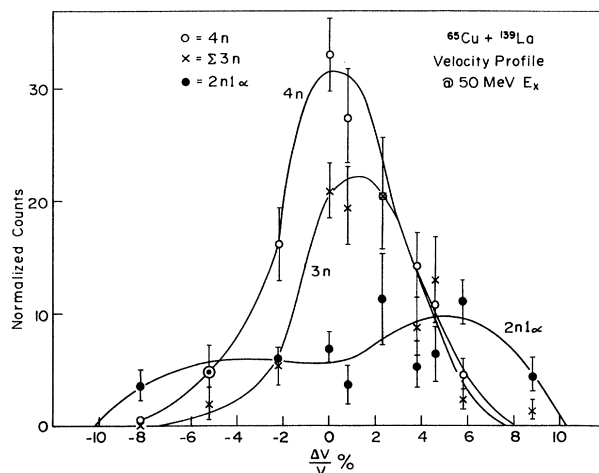

FIG. 9. Zero degree velocity distributions for 3n, 4n, and $2n1\alpha$ evaporation. Error bars are statistical. Note the $2n1\alpha$, 0% minimum which is typical of $xn1\alpha$ evaporations (see the text). Cu + La has the narrowest velocity and angular profiles of the triad, owing to its larger center-of-mass momentum (compare with ^{37}Cl + ^{169}Tm in Ref. 6).
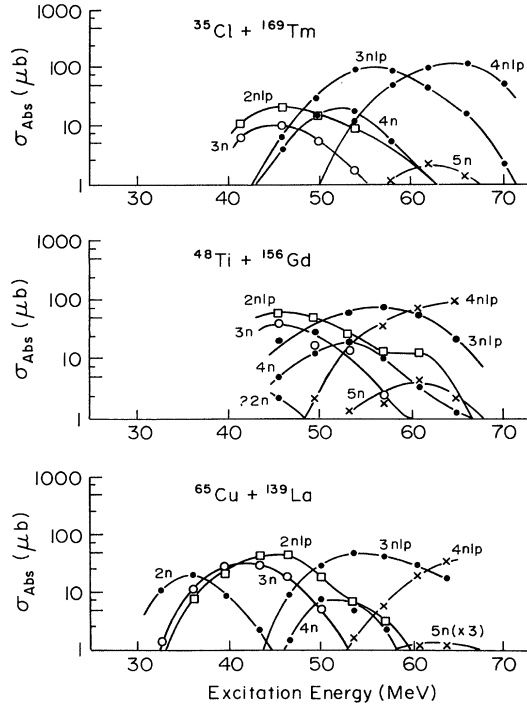
FIG. 10. Absolute excitation functions obtained by rescaling the data of Fig. 8. Curves are only to guide the eye. There are three types of data uncertainty to be considered here: system relative, evaporation mode relative, and overall absolute. Sources of uncertainty and their magnitudes are discussed in Sec. III D.

is obtained since another factor $[1+(\Delta v/v)]^2$ is involved in the conversion.

The absolute cross sections which have been rescaled from the normalized data are shown in Fig. 10. Note the enhancement of the xn1p/xn ratio over the unscaled data ratio reflecting the broader angular distribution for the xn1p evaporation recoil.

D. Sources of error

There are five main contributions to the uncertainty of the data in Fig. 10. The first is statistical and can be found by taking the square root of the counts (Poisson) for each corresponding data point in Fig. 8, then rescaling appropriately for the absolute data error. The second involves an uncertainty in the angular and velocity distributions of the recoils for each evaporation mode. This is negligible at E_{NORM}^{lab} (Fig. 8) where these profiles were measured, but may make contributions as large as the statistical errors farther from E_{NORM}^{lab}. The third error contribution is caused by the uncertainty in the extrapolated velocity selector efficiencies (Sec. II A) for Ti + Gd, Cu + La, and would contribute to their absolute ordinate scale uncertainty by about ±20%. The fourth has to do with the uncertainty in the alpha decay branching ratios for the 4n1p and 5n evaporation ratios. These were assumed to be 100% (Table IV) with no other justification than the trend in neighbor nuclides. The data in Fig. 3 agree well with the corresponding sums in Fig. 10. This is

further confirmation that the alpha branching ratios were chosen appropriately since the Fig. 3 data are derived from the evaporation residue signal alone. The last error source is due to the target contaminants of ^{155}Gd and ^{157}Gd isotopes (about 6% of target) for the ^{48}Ti+^{156}Gd reaction. The most notable distortions are seen in the enhanced 5n cross section as well as the larger 2n1p tail relative to the other reaction systems and ALICE predictions.

In addition to the statistical error for the Fig. 8 data, there is some uncertainty in velocity selector tuning for $0\%(\Delta v/v)$ and in alpha peak separation for 2n1p and 3n1p (see Fig. 6) evaporation residues. These are generally smaller than the statistical uncertainty and can be neglected.

IV. DISCUSSION AND CONCLUSIONS

The excitation function ratios (e.g., 2n1p/3n) in Fig. 10 bear close resemblance between reactions and with the predictions of ALICE (Fig. 7), which is based on the equilibrium model of the compound nucleus. This is strong evidence that a unique compound state of equilibrium has been reached for all three systems. Many tests of this entrance channel independence have been performed for lighter systems (see the review by Hodgson[14]). A more recent paper is that of Hinde *et al.*,[15] where two reactions leading to ^{200}Pb have been studied.

The "cold nucleus" idea failed for this triad of reactions with the results opposite to what this idea predicts. Angular momentum effects in the entrance channel (the $\hbar^2$ factor) clearly dominate in determining the cross-section values.

With appropriate choices for input parameters, general agreement with statistical decay predictions are found for the excitation functions of specific evaporation residues. Parameter choices were 0.8 for the fraction of liquid drop fission barrier used (BARFAC), 1.03 for the single particle level density ratio of the saddle point to the equilibrium deformations (CLD), and $=204/9.5$ for the single particle level density at equilibrium (PLD). Since ALICE does not couple spin, initial populations well above the yrast line are required for meaningful results. When the above parameter choices are used the codes overpredict the xn1α cross sections which only had experimentally determined upper limits. The codes use a single parameter potential (Woods-Saxon) with variable radius parameter only[16] to determine compound nucleus cross sections. This must be used with caution when working in the sub-barrier energy regime, and a more refined method for determining transmission coefficients should be considered.

The gamma multiplicity results demonstrate that even for these low spin and low cross-section experiments, physically meaningful first and second moments of the multiplicity distributions may be obtained. Although the errors on the absolute means may be large, the relative means (between reactions) are well determined and were found to be quite close. This result is consistent with predictions of ALICE and MBII as well as the similarities of the empirical excitation functions that resulted from these similar means.

*Present address: U.S.M.A., Physics Department, West Point, NY 10996.

[1]H. Enge, A. DiRienzo, A. Sperduto, M. Salomaa, S. Gazes, W. Schier, and H. E. Wegner, in Proceedings of the International Conference on Nuclear Physics, Berkeley, 1980, Lawrence Berkeley Laboratory Report LBL-11118, 1980, p. 931.

[2]J. Huizenga and A. Ghiorso, cited in V. E. Viola, Jr. and B. D. Wilkins, Nucl. Phys. 82, 65 (1966).

[3]M. Blann, University of Rochester Report No. COO-3494-32, 1976 (unpublished); F. Plasil and M. Blann, Phys. Rev. C 11, 508 (1973).

[4]M. Beckerman and M. Blann, University of Rochester Report No. UR-NSRL-135A, 1977.

[5]G. E. Schwender and P. C. Rogers, IEEE Trans. Nucl. Sci. 16, 162 (1969).

[6]W. Schier, J. Chervenak, A. C. DiRienzo, H. Enge, D. Grogan, J. Molitoris, M. Salomaa, and A. Sperduto, Phys. Rev. C 23, 261 (1981).

[7]S. B. Kowalski and H. A. Enge, RAYTRACE (unpublished).

[8]M. Beckerman, J. Ball, H. Enge, M. Salomaa, A. Sperduto, S. Gazes, A. DiRienzo, and J. D. Molitoris, Phys. Rev. C 23, 1581 (1981).

[9]S. Y. Van der Werf, Nucl. Instrum. Methods 153, 221 (1978); also A. P. Smith, submitted to Nucl. Instrum. Methods.

[10]H. Gauvin, Y. Le Beyec, M. Lefort, and R. L. Hahn, Phys. Rev. C 10, 722 (1974); M. LeFort, ibid. 12, 686 (1975).

[11]P. Hornshoj, K. Wilsky, P. G. Hansen, A. Lindall, and O. B. Nielsen, Nucl. Phys. A163, 277 (1971).

[12]K. Valli, M. J. Nurmia, and E. K. Hyde, Phys. Rev. 159, 1013 (1967).

[13]P. Hornshoj, P. G. Hansen, and B. Johnson, Nucl. Phys. A230, 380 (1974).

[14]P. Hodgson, Nuclear Heavy Ion Reactions (Oxford University, New York, 1978), Chap. 4, p. 194ff.

[15]D. H. Hinde, J. R. Leigh, J. O. Newton, W. Galster, and S. Hie, Nucl. Phys. A385, 109 (1982).

[16]T. D. Thomas, Phys. Rev. 116, 703 (1959).